

Characterization of Meteorological and Seeing Conditions at Haleakala¹

ELIZA S. BRADLEY,² LEWIS C. ROBERTS, JR., L. WILLIAM BRADFORD, AND MARK A. SKINNER

The Boeing Company, 535 Lipoa Parkway, Suite 200, Kihei, HI 96753; ebradley@fastmail.fm, lewis.c.roberts@boeing.com, lawrence.w.bradford@boeing.com, mark.a.skinner@boeing.com

DAVID A. NAHRSTEDT

The Boeing Company, 8531 Fallbrook Avenue, MS/WB53, West Hills CA 91034-3232; david.a.nahrstedt@boeing.com

AND

MARK F. WATERSON³ AND JEFF R. KUHN

Institute for Astronomy, University of Hawaii, 2680 Woodlawn Drive, Honolulu, HI 96822; waterson@mso.anu.edu.au, kuhn@ifa.hawaii.edu

Received 2005 July 13; accepted 2005 August 31; published 2006 January 5

ABSTRACT. Haleakala is the site for numerous telescopes, but the amount of published information on summit conditions is small. We seek to rectify that by presenting several years' worth of data on weather (cloud statistics, relative humidity, temperature, wind speed, and wind direction) and seeing conditions. We also examine the dependence of seeing on wind. Our goal is to provide observers with information that will help them better choose the timing of their observations, and to build up a climatological record for the site.

1. INTRODUCTION

Haleakala is the third highest mountain in the Hawaiian Islands and experiences excellent conditions for astronomical observing. Located on the island of Maui, its unique orography (topography of a mountain) is characterized by the Haleakala caldera, an erosion feature 9.8 km wide, which is often erroneously referred to as Haleakala crater. The summit of Haleakala is a volcanic cinder cone surmounted by the Haleakala National Park visitor's center. Although the mountain's impressive stature would suggest that its proper name should be "Mount Haleakala," that is incorrect, as Haleakala in native Hawaiian means "House of the Sun," with "Mount" being implicit in this title. The observatory is located at latitude 20°42'30".5 north, longitude 156°15'28".7 west, and an altitude of 3053 m above sea level.

Near the summit of Haleakala are located several telescopes: the Mees Solar Observatory (Mickey 1985), the 2 m MAGNUM (Multicolor Active Galactic Nuclei Monitoring) Project (Kobayashi et al. 2003), the 0.5 m SOLARC (Kuhn & Coulter 2003; Kuhn et al. 2003), the 2 m Faulkes Telescope North (Bedient et al. 2003), the 0.1 m XO Project (McCullough et

al. 2005), and the Maui Space Surveillance Complex (MSSC; Lambert et al. 1999), which includes the 3.63 m AEOS (Advanced Electro-Optical System) telescope (Roberts & Neyman 2002) and the 1.2 and 1.6 m telescopes. The MSSC has two parts: the Maui Space Surveillance System (MSSS) and the Ground-based Electro-Optical Deep Space Surveillance (GEODSS) site. Both are operated by the United States Air Force. Recently, a ComCAM was installed on the mountain. This is one of a series of all-sky cameras installed at observatories across the globe (Perez-Ramirez et al. 2000). Haleakala has also been selected as the site of the future Advanced Technology Solar Telescope (Hill et al. 2002). In addition to the optical telescopes, there is a neutron monitor station (Pyle 2000) and the All-sky Survey High-Resolution Air Shower detector (ASHRA) for cosmic-ray research (J. G. Learned 2004, private communication). The LURE Observatory (Lunar Ranging Experiment; Carter & Williams 1973) was recently removed from the mountain and will be replaced by the temporary home for the first Pan-STARRS (the Panoramic Survey Telescope and Rapid Response System) telescope (Kaiser et al. 2002). Figure 1 shows an aerial view of the mountaintop and the locations of the major telescopes on the mountain.

Given the number of observatories at the summit of Haleakala and the amount of work that has been done over the years to characterize the site, there should be an abundance of published atmospheric seeing and meteorological information pertaining to the site. This is not the case. Several studies have been funded in the past by the Air Force, but their results were not widely disseminated, since MSSS is a nonastronomical observatory. In recent years, more members of the astronomical

¹ Based in part on data from the Maui Space Surveillance System, which is operated by Detachment 15 of the US Air Force Research Laboratory's Directed Energy Directorate.

² Current address: Earth and Environmental Sciences Graduate School and University Center, City University of New York, 365 Fifth Avenue, New York, NY 10016.

³ Current address: Research School of Astronomy and Astrophysics, The Australian National University, Mount Stromlo Observatory, Cotter Road, Weston, ACT 2611, Australia.

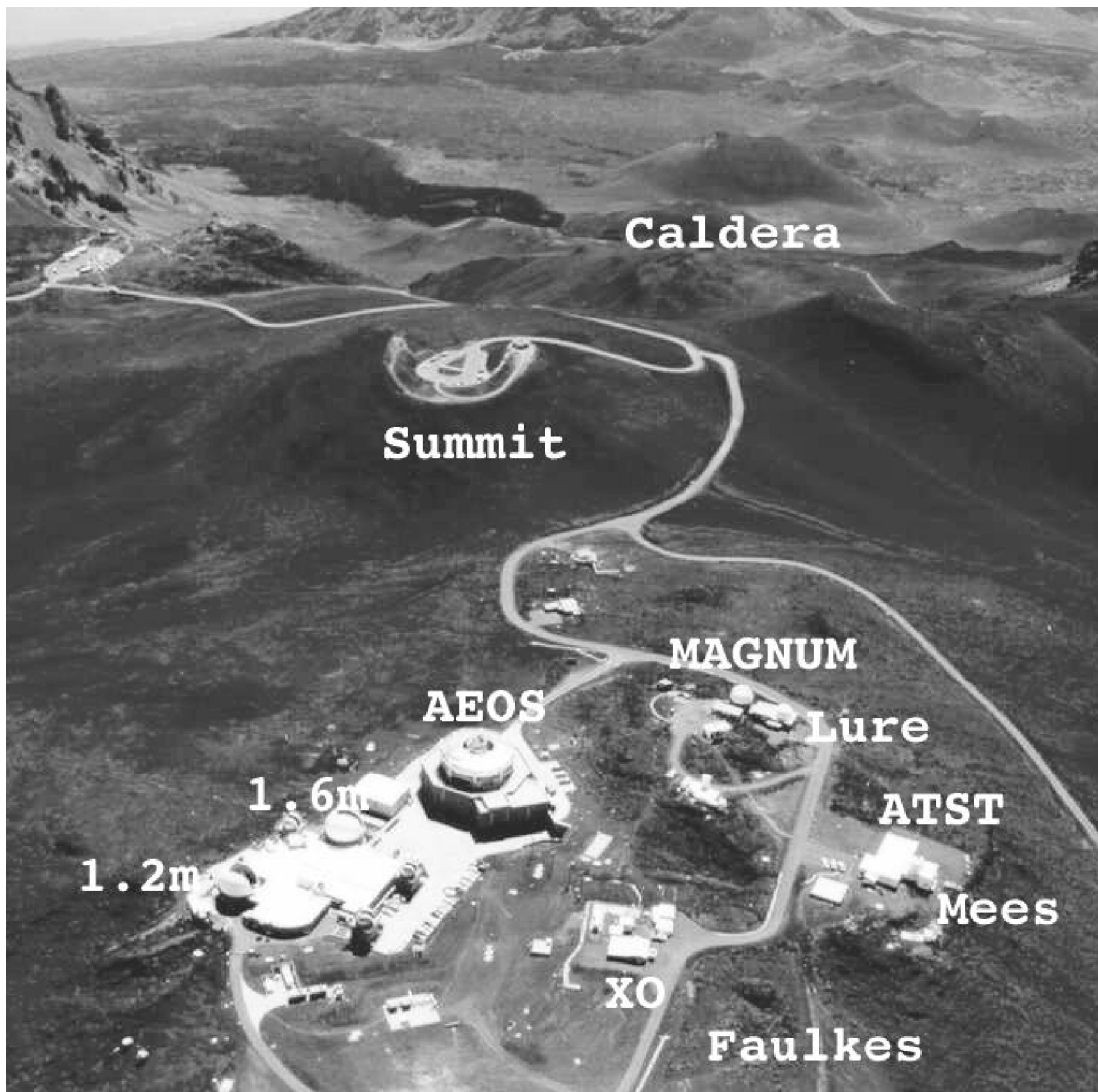


FIG. 1.—Aerial photograph of the summit of Haleakala. The locations of the telescopes mentioned in the text are labeled. The Faulkes telescope postdates the photograph, and its approximate location is identified. The possible site for the ATST is marked, as are the true summit and the caldera. Note that the perspective gives a false impression that other parts of the mountain are higher than the summit.

community have been able to carry out observations with the AEOS telescope. Telescopes are also being added to the mountain at an increasing rate. Our purpose is to make the wider astronomical community more aware of the potential of Haleakala by characterizing the meteorological and seeing conditions at the summit. The information can be utilized to optimize scheduling of observing and for evaluating Haleakala as a site for future telescopes.

We present a summary of the previous 3 years of measurements that are of particular interest to the astronomical community. The meteorological data come from sensors located at the MSSS. Seeing data come from the Day-Night Seeing Monitor operated by the University of Hawaii's Institute for As-

tronomy. Readers interested in aspects of Hawaiian meteorology relevant to astronomy may wish to consult the articles by Erasmus (1986) and Bely (1987).

The Hawaiian Islands, approximately 4000 km from the nearest continental land mass, experience a tropical maritime environment near sea level. However, the steeply rising volcanic mountains, ridges, and ravines provide for a variety of microclimates. Because of the high humidity of the tropical maritime environment, cooling of the air with altitude causes cloud formation, and precipitation at the dew point is common on Haleakala. Clouds tend to form at an inversion layer approximately 1 to 2 km in altitude, providing dry, clean air above the Haleakala summit, with visibility exceeding 150 km. How-

ever, clouds will rise above the summit, due to inversion weakening, temperature differentials, and other factors.

The prevailing winds come from the east and northeast and are commonly referred to as trade winds. Dominating Hawaiian weather conditions approximately 75% of the time, they also tend to cause the windward side of the Islands to experience significantly greater rainfall than the leeward sides. The trade winds are generated by a series of high-pressure anticyclones and ridges, which persist 300–500 miles (450–800 km) north of the islands. From late November through April, the highs and their associated ridges periodically break down or are pushed south by low-pressure systems moving through the North Pacific toward the North American mainland. Fronts and troughs associated with these lows are primarily responsible for Maui's rainy season. Another component of the rainy season is the "Kona" (Hawaiian for leeward side) storm, generated when high-pressure centers move south of the islands and the winds turn southerly, bringing moisture north from the subtropical convergence zone. From July through October, occasional rain and storms are associated with the remnants of hurricanes and tropical storms originating off southern Mexico. These storms typically dissipate to the east of Maui, but a hurricane actually reaches the islands every 5–10 years. Average rainfall at Haleakala is about 15 cm month⁻¹ during winter and spring (November–April) and about 5 cm month⁻¹ in the summer and fall (May–October). Light snowfall occurs rarely, with maximum accretions of 25 cm observed.

Haleakala's upper reaches are defined by a Y-shaped ridge, with the observatories and the summit located at the vertex. One arm of the Y extends to the northeast, while the other runs due east. The base of the Y extends west by southwest. The ridges adjacent to the site drop off steeply. Haleakala's caldera, bounded on the north and south by the arms of the Y, is large, relatively deep, irregularly shaped, and slopes downward toward the east.

The summit area used by the observatories is an elongated area perhaps 300 × 200 m, with the long axis in an east-west direction. The AEOS 3.6 m telescope and the other MSSS telescopes are on the northern boundary, while the academic observatories are along the southern boundary.

The orography factors strongly in the seeing conditions at the site. With the prevailing winds from the east to northeast, air must cross over the caldera before reaching the observatories; this has the effect of increasing the turbulence immediately above the site (this is discussed more in § 3.5.) After a series of site surveys showed the presence of a low-level layer of turbulence, the AEOS telescope facility was designed to sit well above much of the immediate surface layer (Walters et al. 1992).

As is to be expected from fluid dynamics considerations, the presence of a large mountain in the middle of a nearly laminar air stream causes significant flow distortion that may extend well above the peak, both to windward and leeward directions. Gravity waves will be launched upward and create turbulence

at higher altitudes. Nevertheless, the relatively small size of the Hawaiian Islands means that the amount of upper air turbulence generated by interaction with the mountains will be relatively small. However, upper air turbulence due to shears between wind flows (particularly in the presence of a jet stream) may still be present. The overall effect is that good seeing is expected at sites above the local inversion levels. This paper presents data that show that Haleakala's median nighttime seeing corresponds to an image size (FWHM) of 0.7 measured at 500 nm.

2. INSTRUMENTATION

In order to characterize the meteorological conditions of the Haleakala summit, we have relied upon extensive data collected by the Maui Space Surveillance System and the University of Hawaii Institute for Astronomy. Three years' worth of readings for standard meteorological variables, including temperature, relative humidity, barometric pressure, wind speed, and wind direction, are included in this database, as are 2.5 years of atmospheric seeing information.

2.1. Meteorological Equipment

Near-site, 360° azimuthal coverage of basic weather information is provided by three identical sensor suites mounted around MSSS (Skinner et al. 2001). These are located on the north tower (by the 1.2 m dome), on a mast on the south side of the AEOS dome, and about 500 m distant, in the direction of the prevailing winds, on the roof of the Haleakala National Park Service's summit visitor's center. The sensors provide weather information approximately once a second. In the analysis, we utilize data from the north tower, as it is the most reliable of the sensor suites and is best situated to describe conditions at the observatory. We use the other sensors to corroborate the north tower data, and in those instances in which additional information provide insight.

The weather monitoring package consists of several instruments. The anemometers have a range of 0–60 m s⁻¹, a gust survival of 100 m s⁻¹, wind speed accuracy of ± 3 m s⁻¹, and wind direction accuracy of ± 3°. Probes protected by multiplate radiation shields measure relative humidity and temperature. These relative humidity sensors operate optimally between -10°C and 60°C, which includes the temperature range experienced at Haleakala. The error associated with the relative humidity tends to increase at the extremes of its range. At 20°C, accuracy for the sensor is ± 3% from 10% to 90% RH (relative humidity), and ± 4% from 0% to 10% and from 90% to 100% RH. The temperature sensor measures from -50°C to 50°C, with an accuracy at 0°C of ± 0.1°C.

2.2. Day-Night Seeing Monitor

The University of Hawaii's Institute for Astronomy operates a differential image motion monitor (DIMM), known as the Day-Night Seeing Monitor (DNSM), adjacent to the summit

observatories. As the name implies, the device is intended to provide information to both solar and night observers, so it uses bright stars to collect data in the daytime as well as at night. The theory behind the operation of DIMMs is well explained in other sources (Fried 1975; Sarazin & Roddier 1990). Results from the DNSM are discussed below.

The primary telescope optics are all spherical surfaces: a modified Maksutov system consisting of a 40 cm primary mirror, a secondary mirror, and a thick meniscus corrector lens assembly mounted close to the secondary. These optics form a conventional Cassegrain focal plane image of the star through the central perforation in the primary mirror. The DNSM Hartman screen, attached at the front of the telescope tube, contains four 11 cm diameter subapertures in an equally spaced square array with 15.68 cm sides. The use of four subapertures instead of the normal two subapertures provides an increased signal-to-noise ratio. The screen can easily be removed from the front of the telescope tube if necessary. One reason to do this would be to replace it with a screen with different sized apertures. The ancillary optics located in the backplane area form a relayed image of the pupil and hence the subapertures. A precision adjustable optical wedge assembly is located at the pupil image plane. The wedges split the respective pupil beams to form four separate images at the camera.

To enable daytime seeing measurements, we found that placing a red glass filter in the beam reduced the scattered sky light sufficiently to allow us to take data during the day. One consequence of the optical design of the system is that telescope performance is emphasized in the *R* and *I* bands, and the red filter can be left in place for nighttime observations without greatly compromising the instrument sensitivity. The filter is a colored glass Schott filter with a blue cutoff at approximately 600 nm.

At the beginning of 1998 the telescope was moved to its current mount on the unused 10 m cylindrical Zodiacal Light Observatory tower. When not in use, the telescope is housed inside the tower on a deployable platform. During operation, the tower roof is retracted and the instrument is lifted by a hydraulic ram to an indexed position approximately 11 m above ground level. In this location it is largely free from orographic and building turbulence, so that the measurements reflect the true free-atmospheric seeing, unperturbed by dome or localized building effects. The roof and lift system is controlled by a local computer system that uses a decision-tree algorithm to monitor environmental conditions and system performance for faults and potentially adverse conditions. System actions and faults are logged to disk to allow for status monitoring and the diagnosis of errors.

A seeing measurement is computed from a set of 100 images taken at approximately 200 frames s^{-1} . The positions of the four star images are measured in each frame of the set, and the differential motion between frames are computed. The atmospheric conditions required to produce this level of movement are interpolated from a precomputed simulation of the

system and the atmosphere. The computed Fried parameter r_0 is adjusted to 500 nm and to zenith.

The DNSM runs autonomously, operating 21 hr day^{-1} . Operation commences at 2:30 P.M. Hawaiian Standard Time (HST; 00:30 UT) and runs through 11:30 A.M. (21:30 UT) the following morning. The 2 hr shutdown period is to prevent Sun damage to the optics. The DNSM is stowed when not in use. Wind and weather are monitored so that the DNSM can be automatically stowed when adverse conditions occur.

If the wind speed exceeds 13.5 m s^{-1} , or the relative humidity is greater than 85%, or the temperature drops below 0°C , the system will suspend operations and “sleep” for 1 hr. The system requires about 7 minutes to close.

3. METEOROLOGICAL DATA

3.1. Cloud Cover

Cloud cover can have a major impact on the observational ability of ground-based imaging systems.

A major factor in the utility of any site for astronomical observations is the number of days that are lost to cloudy weather. Cloud coverage (*C*) is defined as the cloudy fraction of the sky when viewed vertically. It varies from zero to unity and increases with zenith angle, due to the vertical extent of the clouds and increasing optical depth for a given extinction coefficient. The variation in *C* with zenith angle is sometimes referred to as apparent cloud cover (*S*; J. Snow 1988, unpublished). This implies that $S \geq C$ with $S = C$ at 0° zenith angle (θ_z). The probability of a cloud-free line of sight (P_{CFLOS}) is defined as $1 - S$. In this analysis, $S = C$, since $\theta_z = 0$.

We derived P_{CFLOS} for Haleakala from D. Holland (1993, unpublished). Holland used real-time nephelometer analysis data provided by the USAF Environmental Technical Applications Center, now the Combat Climatology Center. The database contains cloud and weather data compiled from conventional surface stations, upper air stations, and satellites. Observed clouds are placed within four layers for each grid point. The analysis uses a 512×512 polar stereographic grid with a resolution of about 40 km. The data set is global in coverage and available for synoptic hours (00, 03, 06, 09, 12, 15, 18, and 21 UT). The results are shown in Figure 2. There is decreased P_{CFLOS} (greater chance of clouds) during the daytime hours, particularly in the late afternoon until sunset. The average nighttime P_{CFLOS} is about 70%. This drops to about 62% for the daytime average. The greatest P_{CFLOS} (77%) occurs in September, between 0 and 3 HST; the lowest P_{CFLOS} (48%) is in November, between the hours of 15 and 18 HST. The overall average P_{CFLOS} was 66%, with a standard deviation of 5.5%. The diurnal variation, with increased chance of cloud cover during the late afternoon to sunset, may result from the cooling temperatures associated with the time period. While no overt seasonal trend is apparent, summer months (like August) and winter months (like January) seem to be less cloudy; spring and fall months such as March (night) and November

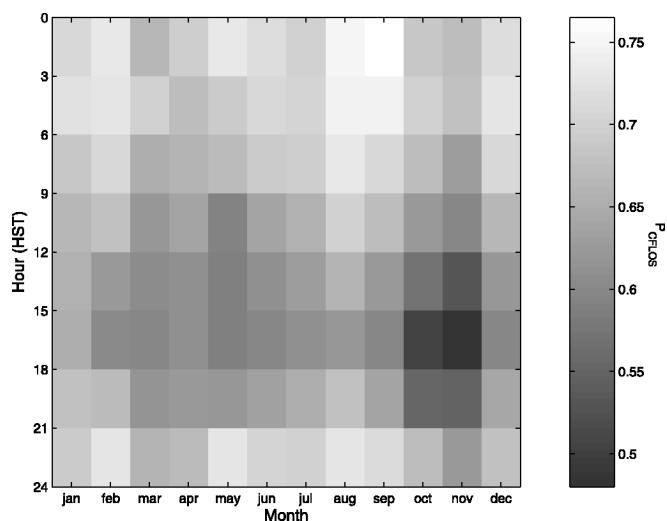


FIG. 2.— P_{CFL0S} as a function of time of day and month for Haleakala. The night has the highest value of P_{CFL0S} ; it is lowest for the time period of 15–18 HST, especially for the months of October and November. Summer months (August) tend to be clearer, as well as winter months (December, January, and February), with intermediate months like March and November typically being cloudier.

(night and day, especially afternoon–evening) tend to be cloudier. These results are in good agreement with the results of Hill et al. (1994), who measured the daytime cloud-free percentage at 64.43% between 1985 and 1991, with a very similar monthly pattern.

3.2. Humidity

Humidity is a major constraint of telescope operations, with high humidity often coexisting with or preceding precipitation and cloud cover. In addition, high humidity reduces atmospheric transmission, due to aerosol scattering and absorption, increases the sky brightness in the near-IR band at night, and raises thermal emissivity due to heat absorption and reradiation over the broader IR band. These effects can result in sensor calibration error in the visible and the infrared. However, the primary motivation for monitoring humidity is to prevent optics from being exposed to moisture. This can lead to oxidation, leaching, and eventual delamination of optical coatings, thus necessitating costly recoating or replacement. At Haleakala, most of the inclement weather prohibiting telescope operation arises from high relative humidity as opposed to high winds, the major concern being the dew-point depression between telescope optics and ambient air.

Investigation into the variation of the median relative humidity as a function of time of day and season resulted in findings that can only support general trends. The lowest median relative humidity was found for spring and summer months (May–July), with the highest humidity months found in winter (January and December). These results correlate well with the

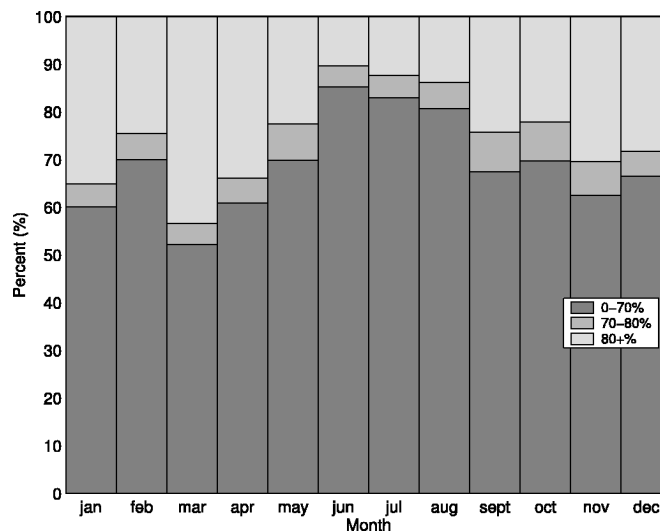


FIG. 3.—Relative humidity distribution as a function of time of day (HST). Diurnal variation of relative humidity is slight, but we do observe a slight decrease in the percent of high humidity during the morning, followed by an increase in the afternoon (with more humidity in the >70% range).

occurrence of the rainy season (November–April) and the dry season (May–October).

Figure 3 shows the diurnal variations in relative humidity and reveals two patterns, the more obvious being an increase in median relative humidity over the daytime period of 11–16 HST. The other pattern, an increase in median relative humidity over the time periods of 04–06 and 21–23 HST, was less prominent and tended to occur when the overall median relative humidity was higher. The lowest median relative humidity tends to occur between 07 and 08 HST.

Analysis of relative humidity distribution as a function of month again follows the pattern of rainy and dry seasons for Haleakala, and is shown in Figure 4. For the months May through September, 90% \pm 3% of the time-relative humidity values are below 80%. For October through April, the probability drops to 80% \pm 5%.

3.3. Wind

Wind can degrade observations by causing telescope jitter and random loading on the mount, causing errors in pointing and tracking, and resulting in overall poor data quality. In addition, high winds increase aerosol concentration and long-range transport, thereby raising the risk of particulate matter being deposited on the optics. This is especially a problem with the volcanic dust present at the summit, which mixes with moisture to form sulfurous acid (HSO_3) and hyposulfuric acid ($\text{H}_2\text{S}_2\text{O}_4$; Nahrstedt et al. 1996). High winds may also increase clear-air turbulence, depending on the time of day and lapse rate (rate the temperature decreases with altitude). In some cases, increased surface wind speed provides better homoge-

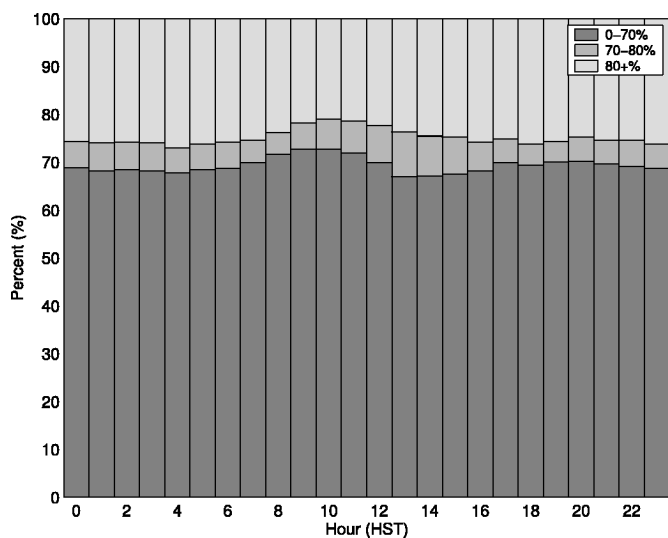


FIG. 4.—Relative humidity distribution as a function of month. The summer months have the greatest concentration of low humidities (0%–70% range) and the least of the high humidities (>80%).

neity, due to the mixing of the thermal layers, thus reducing surface-layer turbulence. Statistically, however, increased wind speed is associated with a decrease in seeing quality.

High winds at Haleakala are often accompanied by an increase in relative humidity. This can be attributed to storm events in which precipitation and high winds are concurrent. The increased winds result in a lifting or disintegration of the inversion layer. This may cause local clouds to rise above the level of the summit. The increase of relative humidity with low wind speed may be the result of advection and convection lifting clouds from the caldera.

The highest median wind speeds at the site occur during the winter and summer. This is consistent with the presence of northeast trade winds in the summer, and stronger but less frequent Kona storms in winter. The mean summer wind speed is 15 m s^{-1} , with a winter mean of 17 m s^{-1} . In intermediate months, such as May, the mean wind speed decreases to about 13 m s^{-1} .

Wind direction at Haleakala is predominately from the northeast to southeast, as shown in Figure 5. This is especially true in the summer months. In the afternoon, wind speeds drop slightly and the wind direction distribution shifts, with an increase in the westerly winds and a decrease in the easterlies.

3.4. Temperature

Air temperature at Haleakala displays normal seasonal and diurnal variations. As shown in Figure 6, the highest temperature occurs midday in September (15°C), and the lowest median temperatures are during the winter months (November–March) at night. The largest seasonal difference in median temperatures, 7°C , slightly exceeds the largest diurnal differ-

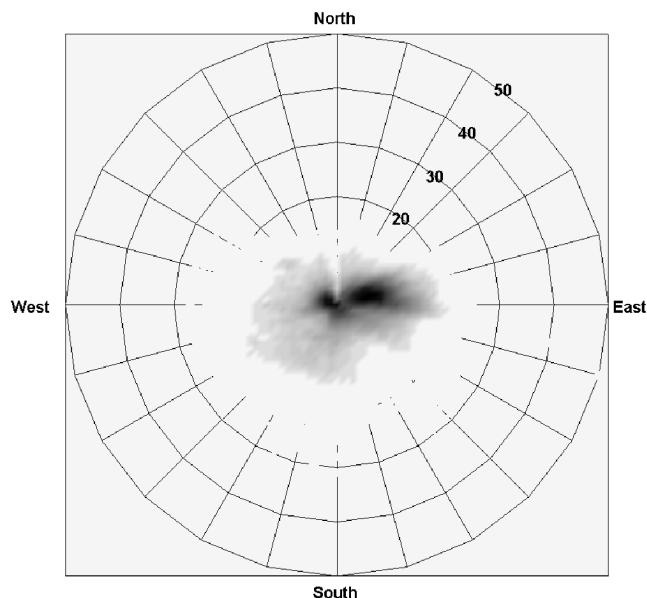


FIG. 5.—Wind speed/direction distribution. The radial axis corresponds to wind speed in units of m s^{-1} . The azimuthal axis corresponds to wind direction. The intensity of the plot indicates the number of data points at a given combination of wind speed and wind direction. A majority of the high speed wind comes from the east. The deficit of points to north is an instrumental effect.

ence, 6°C . The temperature at Haleakala ranges from below -10°C to above 20°C .

3.5. Seeing

One of the key parameters in choosing a site for an astronomical telescope is the seeing. Site-specific seeing is due to

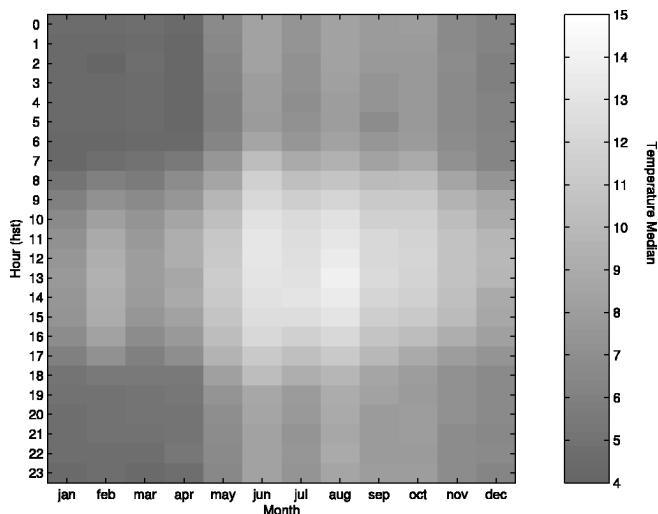


FIG. 6.—Gray-scale image of median temperature as a function of time of day and month. September is typically the warmest month; November–March are the coolest. The median temperature range is from 4°C to 15°C .

TABLE 1
HALEAKALA SEEING CAMPAIGNS

Reference	Technique	r_0 (cm)
Zirkind (1965)	Star trails	28 ± 15
Greenwood et al. (1976)	DIMM, acoustic sounders	8.9 ± 5
Miller & Zieske (1978)	MTF	9.5 ± 2.1
Brown & Good (1984)	Balloon thermosondes	8.3 ± 0.9
Beland et al. (1988)	Balloon thermosondes	13.3 ± 6.5
Walters & Bradford (1997)	MTF	12.9 ± 4
Kuhn et al. (1999)	DIMM	11 ± 4^a
This paper	DIMM	14.7 ± 6.3

^a A combination of daytime and nighttime measurements.

(1) turbulence in the free atmosphere, (2) turbulence in the atmospheric boundary layer (the volume within about 300–1000 m of the surface), and turbulent mixing (3) within and around the dome, and (4) within the telescope optical path. Isolation of each source requires simultaneous measurements with multiple sensors. For example, the FWHM of a star image will be influenced by all four, but a DIMM will be relatively insensitive to the last two local conditions.

Clear-air turbulence is caused by incomplete mixing of the thermal layers in the atmosphere, resulting in velocity, density, and refractive index perturbations. The effects on imaging and tracking include (1) jitter due to variations in index of refraction over transverse scale lengths comparable to the aperture diameter, and (2) image distortion and blur due to higher spatial frequency distortions. Scintillation due to wave-front interference from strong index perturbations at high altitude may cause variations in the image irradiance distribution.

Historically, astronomers have characterized seeing by the FWHM of a star image. However, this includes effects not due to atmospheric turbulence, such as optical system wave-front error and possible image blur due to telescope jitter. The prevailing measure of the impact of atmospheric turbulence on seeing is given by Fried's parameter r_0 , also referred to as the coherence diameter (Fried 1966). It is defined by the equation

$$r_0 = \left[1.692 \pi^2 \lambda^{-2} \sec(\theta_z) \int C_n^2(h) dh \right]^{-3/5}, \quad (1)$$

where λ is the wavelength and θ_z is the zenith angle. The refractive index structure constant C_n^2 arises from the Kolmogorov model of turbulence (Kolmogorov 1941). For a range of physical sizes of turbulent eddies, known as the inertial range, Kolmogorov defines a structure function for some physical quantity X , such as velocity, temperature, or index of refraction, as

$$D_X(r) = |\langle X(\mathbf{r} + \mathbf{y}) - X(\mathbf{y}) \rangle|^2 = C_X^2 r^{2/3}. \quad (2)$$

In a perfectly isotropic, homogeneous medium, C_X^2 would be constant over the medium, and the variance of X would depend only on the separation r . In reality the atmosphere is

neither homogeneous, isotropic, nor stationary at any scale of interest to the astronomer observing an object over time spans of minutes to hours. This means that r_0 can vary over time, and from one point on the sky to another. Fried's parameter thus represents the integrated effect of turbulence along a propagation path. The larger the value of r_0 , the less turbulence encountered and the better the seeing. The usual interpretation of r_0 is that it represents the largest diameter over which a telescope aperture will have a diffraction-limited resolution. Thus, when the r_0 is reported as 10 cm, a 10 cm diameter telescope has the same resolution as a 10 m telescope for a long exposure image.

The seeing at MSSS has been characterized many times over the years, from the early 1960s through the present (Zirkind 1965; Greenwood et al. 1976; Miller & Zieske 1978; Brown & Good 1984; Beland et al. 1988; Walters & Bradford 1997). The original site study indicated excellent seeing, but over the years opinion on the seeing has varied, leading to additional measurements, with campaigns lasting from days to years. Techniques to measure seeing have ranged from star trail measurements (Zirkind 1965), fine-wire anemometers, acoustic sounders, and differential image motion with photographic plates (Greenwood et al. 1976), to modulation transfer function-based methods (Miller & Zieske 1978), balloon-borne thermosondes (Brown & Good 1984; Beland et al. 1988), and differential image motion monitors (CCD camera-based; this paper). Much of the measurement data are buried in reports that are not easily available to the public. In addition, since these studies were conducted, additional mountaintop construction has occurred, which has the potential to affect local seeing conditions.

The results from the various measurements have been mixed, and in some cases it is hard to assign error bars to the data. Zirkind (1965) presents data from 72 observations over a 11 month period, indicating a median seeing equivalent to an r_0 of 28 ± 15 cm, with a standard deviation of 0.38. When later observations failed to support this kind of seeing, an investigation of the seeing was undertaken by Greenwood et al. (1976). They showed 24 observations for seven nights in 1974 August, using the differential image motion technique. Their median value of r_0 (scaled to 500 nm) was 8.9 cm, with a standard deviation of 5 cm. Miller & Zieske (1978), using the Hughes seeing monitor described in their paper, reported 24 values from 1975 November through 1976 July, with a median r_0 of 9.5 cm and a standard deviation of 2.1 cm. Data collected with the Hughes seeing monitor from 1985 to 1990, as reported in Walters & Bradford (1997), had a median r_0 of 12.9 cm and a standard deviation of 4 cm. Brown & Good (1984) used balloon-borne thermosondes to measure r_0 as 8.3 ± 0.9 cm. Later measurements with the same technique produced a result of 13.3 ± 6.5 cm (Beland et al. 1988). Kuhn et al. (1999) collected 1 year of data with the DNSM and produced a combined r_0 of 11 ± 4 cm for a combination of day and nighttime observations. These results, as well as the current results, are summarized in Table 1.

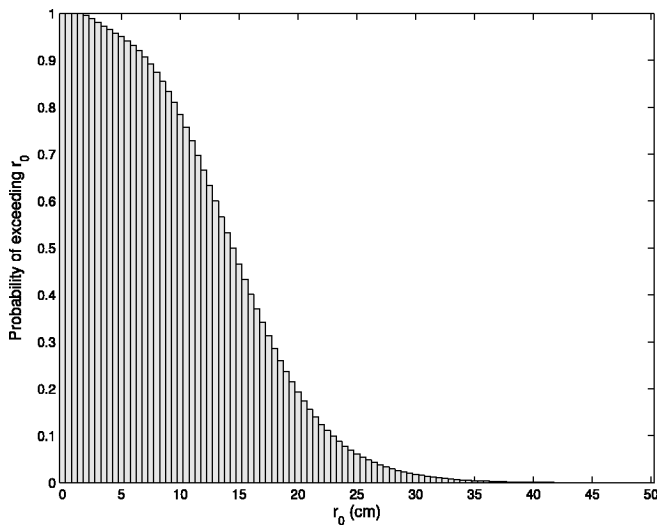


FIG. 7.—Probability exceedance function of r_0 for nighttime measurements. The median value of r_0 is 14.7 cm. The plot is the result of 198,225 measurements by the DNSM during the hours between local sunset and local sunrise from 2002 January to 2004 August, for a total of 662 nights.

The Hughes Seeing Monitor, in use on Haleakala from about the mid-1970s until the early 1990s, was a unique optical instrument that sampled star images on a millisecond timescale and provided information on atmospheric seeing conditions. In this system, star images were scanned in orthogonal directions by a spinning reticle wheel, and the light transmitted through the wheel was processed to yield the modulation transfer function (MTF) of the atmosphere, the seeing angle, and image wander information. The value of r_0 was obtained by the application of Fried's expression for the short-exposure modulation transfer function (Fried 1966)

Using the DNSM data for r_0 , we present observations on the seasonal and diurnal variation of r_0 , as well as its relationship to wind speed and direction. We have divided the data from the DNSM into nighttime and daytime measurements for the period 2002 January through 2004 August. In this paper, night measurements are those made from local sunset to local sunrise, and day measurements are those made between local sunrise and local sunset.

Figure 7 shows the probability that a particular value of r_0 will be exceeded during the night. The median value is 14.7 cm, with a standard deviation of 6.3 cm. There are 198,225 measurements over 662 nights. The differences between these values and those reported by prior measurements may be in part due to the location of the sensors (in particular, proximity to the ground) and to dome turbulence affecting the older measurements. Differences in time of day of the sampled data may also affect the difference. Moreover, the prior data sets reported above reflect only a few thousand measurements (at most).

We have also examined the daytime measurements of r_0 , seen in Figure 8. The data consist of 92,307 measurements taken on 651 days (measured from local sunrise to local sunset).

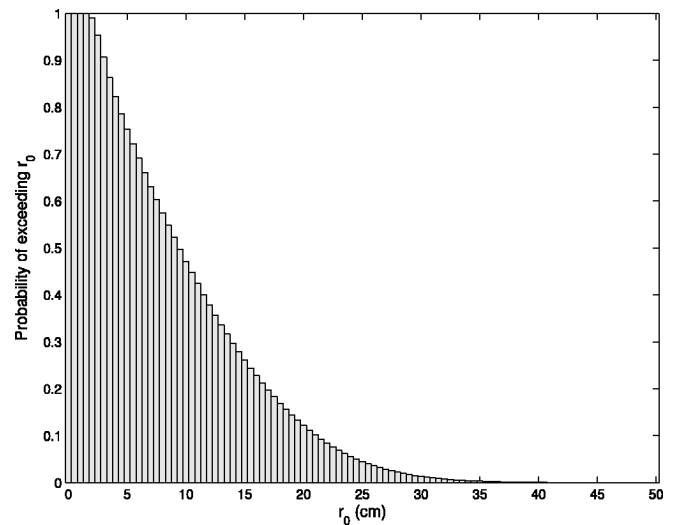


FIG. 8.—Probability exceedance function of r_0 for daytime measurements. The median value of r_0 is 9.7 cm. The plot is the result of 92,307 measurements by the DNSM during the hours between local sunrise and local sunset for 651 days from 2002 January to 2004 August.

The data are incomplete, as there are no data for the 2 hr period centered on local noon, when the DNSM shuts down to avoid damage from the Sun. The median r_0 is 9.7 cm, with a standard deviation of 7.1 cm. Because there is a floor of 2.5 cm (the DNSM does not measure values below this) and the data around local noon is not taken, the median value is somewhat biased to larger r_0 as compared to a complete data set. The daytime data contain a number of high values of r_0 . These are mostly from the very early morning, when the air is still quite stable. However, the measurements of r_0 must be corrected to the zenith angle of the Sun to get a true estimate of what the solar seeing would be like. If r_0 is measured as 15 cm for a star near zenith, then for the Sun observed at 10° above the horizon, the effective r_0 would be 5.3 cm.

We show the monthly distributions of r_0 for night in Figure 9 and for day in Figure 10. The data set is too limited to draw strong conclusions about the distribution of seeing. However, the stable air in the summer months leads to diurnal variations that differ in the shape of the hourly distribution as well as magnitude of r_0 .

From Figure 11, the best seeing is typically during early morning hours. This is a well-known (but largely anecdotal) observation at many observatories. It can be attributed to the stabilization of temperature over the night, resulting in equilibrium between the air and ground temperatures. There are generally two such “neutral” events during a diurnal cycle. One occurs about an hour after sunrise, and the other an hour before sunset. The data show that the dawn neutral event is more prolonged than the dusk event. As the Sun heats up the atmosphere, the seeing quickly degrades.

We also investigated the correlation between r_0 and surface meteorological conditions. Figures 12 and 13 show the r_0 dis-

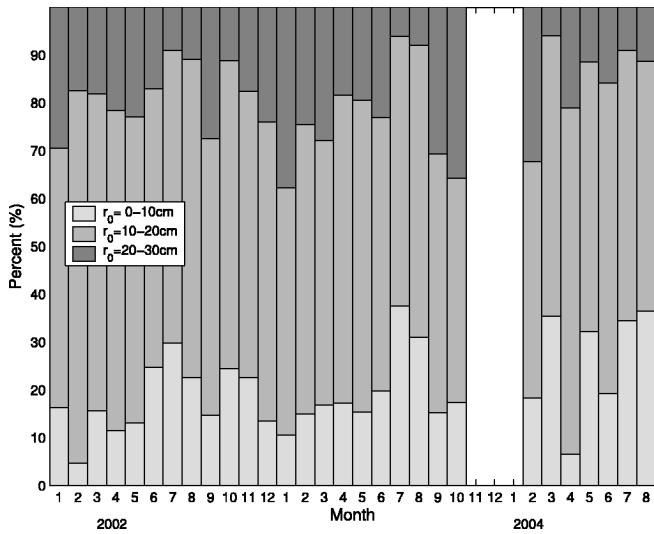


FIG. 9.—Fried's parameter as a function of month for measurements made between sunset and sunrise by the DNSM. It shows the probability distribution for different qualities of seeing: 0–10, 10–20, and 20+ cm.

tribution as a function of wind direction. It appears that the worst seeing, defined as the highest percentage of 0–10 cm r_0 values, occurs when the wind is between 60° and 90° north. Wind from this direction passes through and over the caldera, which leads to an increase in turbulence and poorer seeing. This directional variation is more noticeable for the night measurements than for the day measurements.

The data for Figures 14 and 15 are abbreviated, because the DNSM does not operate at high wind speeds. The figure implies that seeing generally degrades as wind speed increases. Nev-

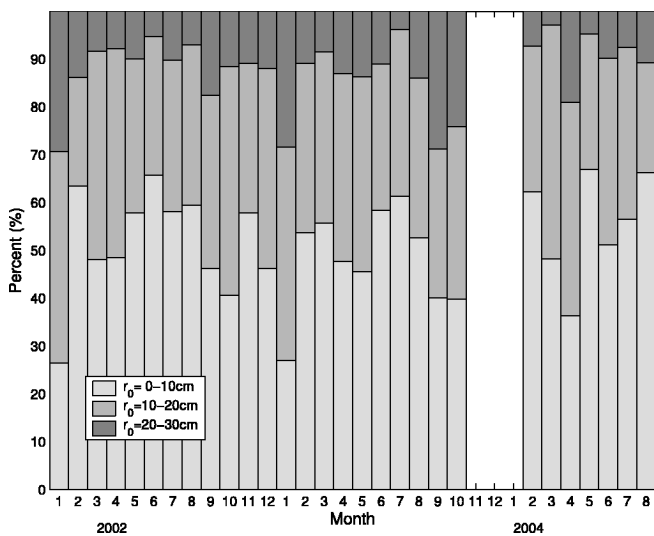


FIG. 10.—Fried's parameter as a function of month for measurements made between sunrise and sunset by the DNSM. It shows the probability distribution for different qualities of seeing: 0–10, 10–20, and 20+ cm.

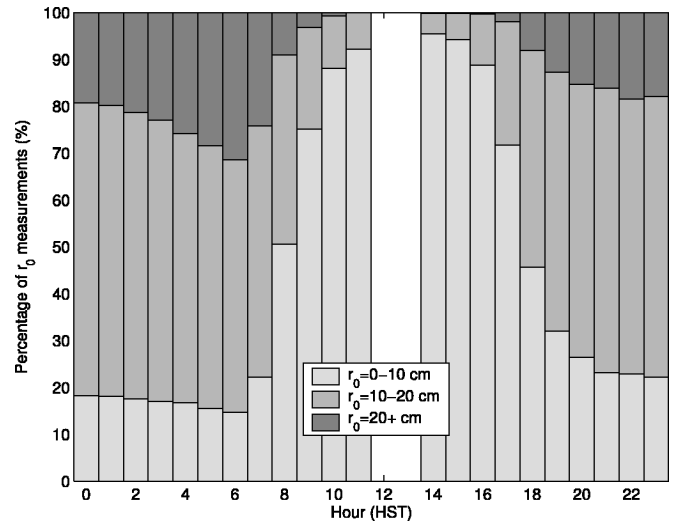


FIG. 11.—Distribution of r_0 the 24 hr diurnal cycle. There are no data collected during the midday hours when the DNSM shuts down. The poorest seeing occurs between late morning and afternoon (approximately 7–20 HST). Late night and early morning have the best seeing.

ertheless, there are some instances of relatively good seeing at higher wind speeds, so the rule is not absolute. In certain situations, high winds lead to thorough mixing of the different thermal layers. In this case, the temperature structure function $C_T^2(r) = \langle [T(\mathbf{y} + \mathbf{r}) - T(\mathbf{y})]^2 \rangle$ is reduced, leading to smaller index of refraction variations. The degradation with increasing wind speed is steeper at night than during the day. During the day, solar heating is the dominant factor in seeing degradation,

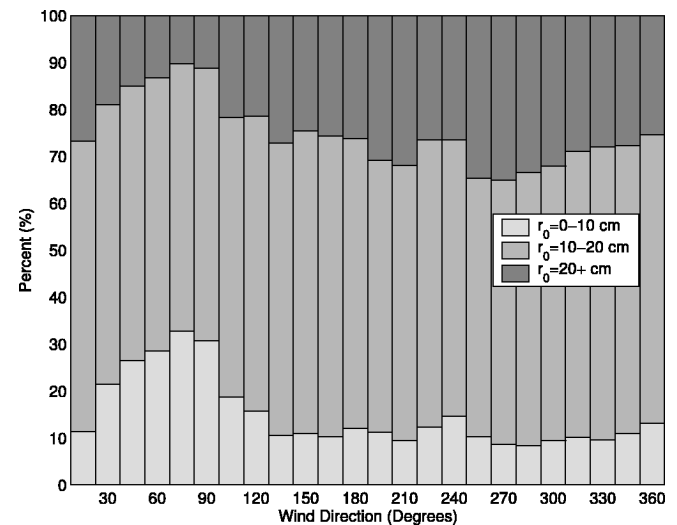


FIG. 12.—Nighttime distribution of r_0 as a function of wind direction (15° bins). The worst seeing occurs when the wind is coming from 60° to 90° north, when the wind comes across the Haleakala caldera. Data are from local sunset to local sunrise.

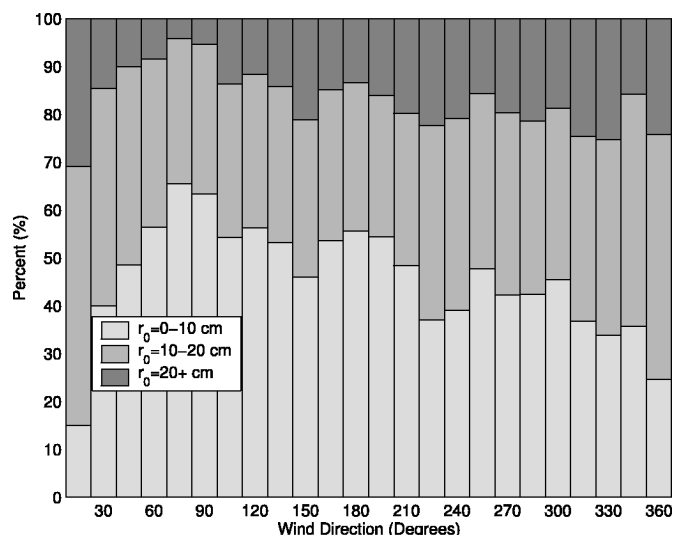


FIG. 13.—Daytime distribution of r_0 as a function of wind direction (15° bins). The worst seeing occurs when the wind is coming from 60° to 90° north, when the wind comes across the Haleakala caldera. Data are from local sunrise to local sunset.

while at night, wind plays a much more important role. It appears that at some wind speed above 15 m s^{-1} , the difference between night and day seeing is moot.

The data also show a strong correlation between poor seeing and low air pressure. This is expected, since low pressure is associated with cold fronts and unstable air. The arrival of a cold front has been noted to cause seeing to worsen as the front moves through. There is no obvious correlation with pressure above 708 mm Hg.

4. SKY BRIGHTNESS

The daytime sky brightness at Haleakala has been monitored for more than 45 years (LaBonte 2003). LaBonte reports a median brightness per air mass of 10 millionths of the solar disk, with a mode of 5 millionths. This corresponds to a very dark sky, with Rayleigh scattering being only 1 millionth of the solar disk. The night sky is also dark, but light pollution is a growing concern as the island communities increase in population. The clouds at the inversion layer will sometimes attenuate some of the line-of-sight light pollution. Attempts to encourage communities to adopt antilight-pollution measures have started but are encountering some resistance from local law enforcement and commercial interests (Wainscoat 2003). Measurements at Haleakala indicate that the primary source of thermal infrared background emission is from water vapor (Kent & Korff 1982). The temporal power spectral density for the sky radiance background fluctuations are analyzed in Nahrstedt & Brinkley (1995). The daytime sky transparency variations over 6 years were reported in Hill et al. (1994).

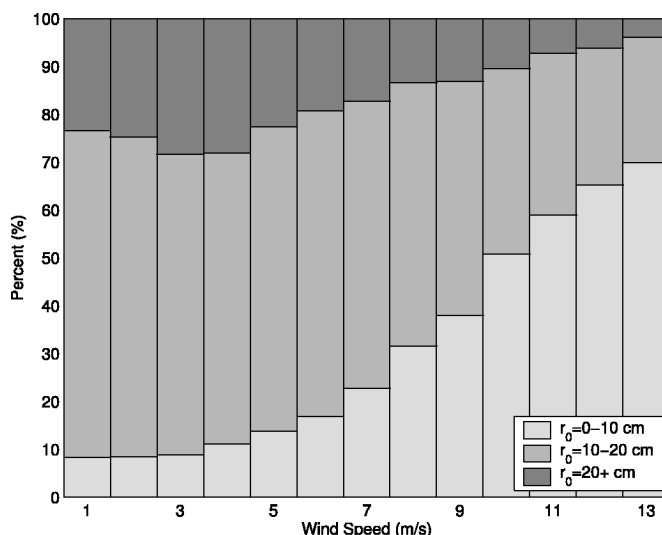


FIG. 14.—Distribution of r_0 as a function of wind speed during the night. At the higher wind speeds, there is a lower probability of good seeing ($20+$ cm) and a significant increase in poorer seeing ($0-10$ cm range). Data is from local sunset to local sunrise.

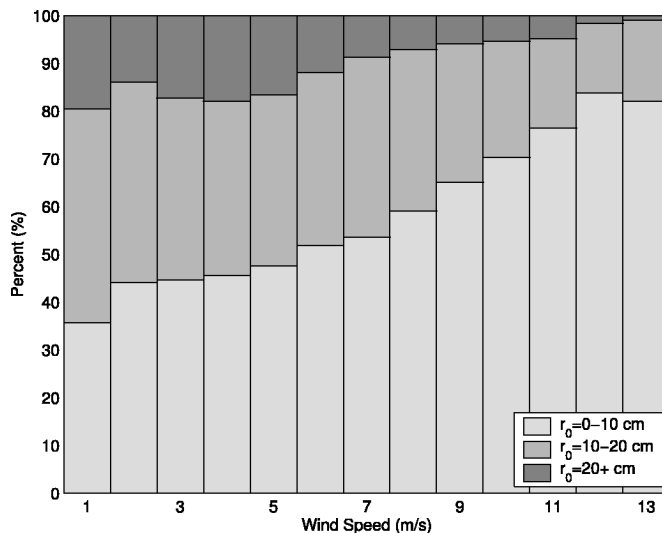


FIG. 15.—Distribution of r_0 as a function of wind speed during the day. The increase in poor seeing with wind speed is perhaps less dramatic than for night conditions, because the seeing is poorer to start with. Data is from local sunrise to local sunset.

5. SUMMARY

We have presented median trends and distributions based on an analysis of long-term measurements of meteorological and seeing parameters at the summit of Haleakala. In addition, we have described diurnal and seasonal correlations between parameters. The data and analysis summaries presented here should help experimenters more efficiently and effectively plan observations at the Haleakala observatories.

We would like to thank the staff of the Maui Space Surveillance System for their invaluable assistance. Malcolm Northcott provided invaluable assistance in the design and creation of the DNSM. The referee, René Racine, and our colleague, Marshall Perrin, both provided a helpful critique of the paper, which improved the paper. This work was funded by AFRL/DE (contracts F29601-00-D-0204 and F29601-98-K-0149).

REFERENCES

- Bedient, J., Meech, K. J., Kadooka, M. A., Mattei, J. A., Hamai, J., Hemphill, R., & Hu, S. 2003, *BAAS*, 35, 42.01
- Beland, R. R., Brown, J. H., Good, R. E., & Murphy, E. A. 1988, *Optical Turbulence Characterization of AMOS*, 1985 (AFGL-TR-88-0153; Hanscom AFB: Air Force Geophys. Lab.)
- Bely, P. 1987, *PASP*, 99, 560
- Brown, J. H., & Good, R. E. 1984, *Thermosonde C_n^2 Measurements in Hawaii* (AFGL-TR-84-0110; Hanscom AFB: Air Force Geophys. Lab.)
- Carter, W. E., & Williams, J. D. 1973, in *The Earth's Gravitational Field and Secular Variations in Position*, ed. R. S. Mather & P. V. Angus-Leppan (Sydney: Univ. New South Wales), 433
- Erasmus, D. A. 1986, *PASP*, 98, 254
- Fried, D. L. 1966, *J. Opt. Soc. Am.*, 56, 1372
- . 1975, *Radio Science*, 10, 71
- Greenwood, D., et al. 1976, *AMOS Seeing Quality Measurements*, Rome Air Development Center Tech. Rep. (RAD-TR-75-295)
- Hill, F., Briggs, J., Radick, R., & Hegwer, S. 2002, *BAAS*, 34, 734
- Hill, F., et al. 1994, *Sol. Phys.*, 152, 351
- Kaiser, N., et al. 2002, *Proc. SPIE*, 4836, 154
- Kent, H., & Korff, D. 1982, *Measurement of Infrared Sky Noise*, Avco Everett Res. Lab. Tech. Rep. (AERLTR-131)
- Kobayashi Y., et al. 2003, *Proc. SPIE*, 4837, 954
- Kolmogorov, A. N. 1941, *Dokl. Akad. Nauk. SSSR*, 30, 9
- Kuhn, J. R., & Coulter, R. 2003, *Eos*, 83, SH41D-06
- Kuhn, J. R., Coulter, R., Lin, H., & Mickey, D. L. 2003, *Proc. SPIE*, 4853, 318
- Kuhn, J. R., Waterson, M., Northcott, M., Maberry, M., & Tokunaga, A. 1999, in *Proc. AMOS Tech. Conf.* (Kihei: Maui Economic Development Board), 85
- LaBonte, B. 2003, *Sol. Phys.*, 217, 367
- Lambert, J. V., Africano, J. L., Talent, D. L., Sydney, P. F., Soo Hoo, V., Nishimoto, D. L., & Kervin, P. W. 1999, *BAAS*, 31, 838
- McCullough, P. R., Stys, J. E., Valenti, J. A., Fleming, S. W., Janes, K. A., & Heasley, J. N. 2005, *PASP*, 117, 783
- Mickey, D. L. 1985, *Sol. Phys.*, 97, 223
- Miller, M. G., & Zieske, P. L. 1978, *J. Opt. Soc. Am.*, 67, 1680
- Nahrstedt, D., & Brinkley, T. 1995, *Opt. Eng.*, 34, 1793
- Nahrstedt, D., Glesne, T., McNally, J., Kenemuth, J., & Magrath, B. 1996, *Appl. Opt.*, 25, 3680
- Perez-Ramirez, D., Nemiroff, R. J., Pereira, W. E., Rafert, J. B., & Ftaclas, C. 2000, *BAAS*, 32, 1599
- Pyle, R. 2000, *Space Sci. Rev.*, 93, 381
- Roberts, L. C., Jr., & Neyman, C. R. 2002, *PASP*, 114, 1260
- Sarazin, M., & Roddier, F. 1990, *A&A*, 227, 294
- Skinner, M. A., Sylva, A., Figgis, P., Chessier, D., Brehm, R. A., & Angara, A. 2001, in *Proc. AMOS Tech. Conf.*, ed. P. Kervin, L. Bragg, & S. Ryan (Kihei: Maui Economic Development Board), 80
- Wainscoat, R. J. 2003, in *Light Pollution: The Global View*, ed. H. E. Schwarzs (Dordrecht: Kluwer), 111
- Walters, D. L., & Bradford, L. W. 1997, *Appl. Opt.*, 36, 7876
- Walters, D. L., Gast, V. J., Mattingly, T. S., & Galarowicz D. 1992, *Adaptive Optics for Large Telescopes Technical Digest*, 19, 17
- Zirkind, R. 1965, *Appl. Opt.*, 4, 1077